Materials & Design 229 (2023) 111929

Contents lists available at ScienceDirect

Materials & Design

journal homepage: www.elsevier.com/locate/matdes

On the elastic microstructure of bulk metallic glasses

Birte Riechers [a], Catherine Ott [b], Saurabh Mohan Das [c], Christian H. Liebscher [c], Konrad Samwer [d], Peter M. Derlet [e], Robert Maaß [a,b,*]

[a] Federal Institute of Materials Research and Testing (BAM), Unter den Eichen 87, 12205 Berlin, Germany
[b] Department of Materials Science and Engineering, University of Illinois at Urbana-Champaign, Urbana, IL 61801, USA
[c] Max-Planck-Institut für Eisenforschung, Max-Planck-Strasse 1, 40237 Düsseldorf, Germany
[d] I. Physics Institute, University of Göttingen, Friedrich-Hund-Platz 1, 37077 Göttingen, Germany
[e] Condensed Matter Theory Group, Paul Scherrer Institute, 5232 Villigen, Switzerland

HIGHLIGHTS

- Elastic properties of a Zr-based bulk metallic glass were probed by spatially resolved nanoindentation.
- An elastic microstructure is observed with fluctuations at a decorrelation length scale of 170 nm.
- Spatially resolved compositional analysis excludes chemical modulations to generate the elastic fluctuations.
- The elastic length scale is connected to local density fluctuations that emerge due to cooling constraints during casting.
- The emerging elastic length scale suggests the formulation of a structure–property relationship for bulk metallic glasses.

GRAPHICAL ABSTRACT

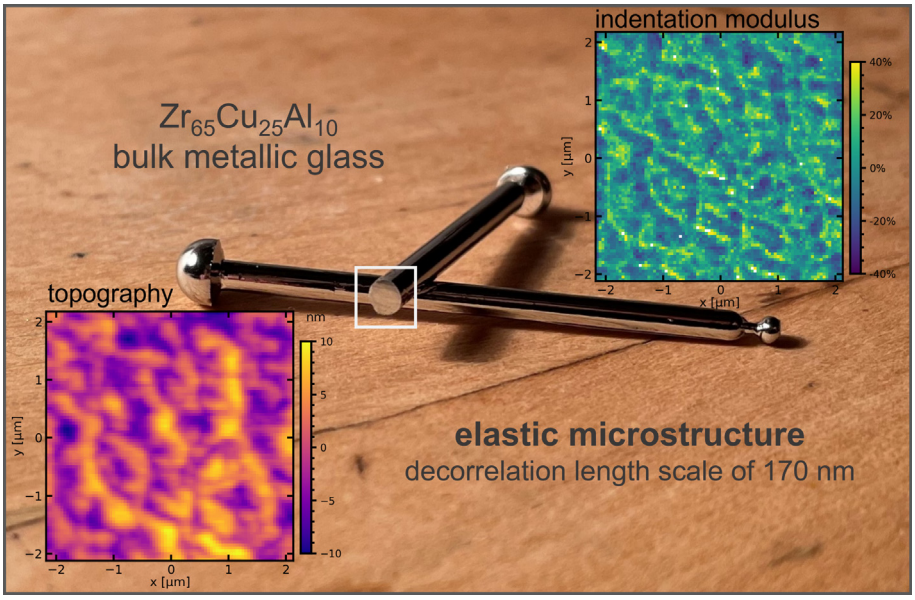

ARTICLE INFO

Article history:
Received 23 February 2023
Revised 5 April 2023
Accepted 6 April 2023
Available online 8 April 2023

Keywords:
Nanoindentation

ABSTRACT

Metallic glasses (MGs) are known to be structurally heterogeneous at the nanometer (nm) scale. In addition, elastic property mapping has indicated the presence of at least an order-of-magnitude larger length scales, of which the origin continues to remain unknown. Here we demonstrate the existence of an elastic decorrelation length of the order of 100 nm in a Zr-based bulk MG using spatially resolved elastic property mapping via nanoindentation. Since compositional modulations, sufficiently large to account for this elastic microstructure, were not resolved by analytical scanning-transmission electron microscopy, chemical phase separation such as spinodal decomposition cannot explain their presence. Instead, we argue that the revealed long-range elastic modulations stem from structural variations affecting the local

* Corresponding author.
E-mail address: robert.maass@bam.de (R. Maaß).

https://doi.org/10.1016/j.matdes.2023.111929

Bulk Metallic Glass
Elastic Microstructure
Structure-Property Relationship

density. These emerge during solidification and are strongly influenced by the cooling constraints imposed on bulk MGs during the casting process.

1. Introduction

Undercooling a metallic melt and bypassing crystallization allows forming metallic materials with a disordered structure, also referred to as metallic glasses (MGs). Casting an MG is only possible for a selected range of multicomponent systems, but irrespective of their detailed chemistry or glass forming ability, MGs have in common that their atomic structure exhibits some degree of short- or medium-range order and therefore heterogeneity [1]. Such local ordering is typically associated with nearest neighbor atoms or the connectivity of polyhedra that may form a network of, for example, icosahedral or Frank-Kaspar type motifs [2,3].

The development of interconnected clusters can conveniently be tracked in atomistic simulations, revealing the emergence of structural length scales and heterogeneity that can be controlled via careful thermal protocols [4,5]. At the experimental scale the situation is more challenging, as most probes are unable to resolve the structural length scales quantified in atomistic simulations. Despite this scale mismatch, a number of efforts have reported (an)elastic property fluctuations that span from the nanometer (nm) to the micrometer (μm) scale [6].

Indeed, for Zr-based MGs correlation lengths, ξ, between 1 and 10 nm have been revealed using amplitude-modulated or acoustic atomic force microscopy (AFM) [7–12], and approx. 150 nm was obtained using indentation modulus mapping [13]. For non-Zr-based MGs, AFM-methods tend to yield slightly higher correlation lengths of a few tens of nm [10,11,14,15], and in one case several μm large elastic length scales were derived from conventional automated nanoindentation on a Pd-based MG [16]. Being present across orders of magnitudes, elastic property fluctuations revealed by nano-mechanical contact methods nurture a picture of a hierarchical landscape of elastic heterogeneities. Being far from understood, we proposed earlier [6] that if (an)elastic length scales are truly representing fluctuations of a unique structural state, an opportunity arises to formulate length-scale based structure–property relationships for MGs similar to those that have enabled the success of crystalline alloys [17,18].

Whilst these developments are exciting, there is effectively only one effort demonstrating a spatially mapped $\xi > 100$ nm [13], of which the origin remains completely unclear. This unsatisfactory situation both in terms of data-scarcity and physical origin needs to be overcome to quantify and eventually exploit the concept of a hierarchical elastic microstructure in MGs. To this end, we set out to i) scrutinize $\xi > 100$ nm and to ii) address if elastic modulus variations may be linked to a spinodal decomposition that for sufficiently slow cooling rates can give rise to clearly identifiable chemical heterogeneity length scales [19].

We probe nano-mechanically the spatially resolved elastic response of a polished Zr-based ($Zr_{65}Cu_{25}Al_{10}$) bulk MG. Whilst a correlation length of the order of 100 nm indeed can be revealed, it is shown that local modulus and topography are correlated quantities, because long-range height fluctuations as small as a few nm clearly affect the nano-mechanical elastic contact. However, considering appropriate corrections for surface curvature, we demonstrate that the identified elastic heterogeneities are intrinsic to the material. In concert with spatially mapped analytical scanning transmission electron microscopy (STEM) and energy-dispersive X-ray spectroscopy (EDS), we can exclude compositional modulations as the origin of the elastic fluctuations. Consequently, variations in structure and thus in local density, which strongly affect the elastic modulus and emerge during the solidification process, are most likely the origin of the long-range signatures found here. These results strengthen the existence of a hierarchical elastic microstructure in MGs and highlight the potential of its characterization using high-throughput nanoindentation-based spatial property mapping.

2. Methods

Automated spatial mapping of local elastic contacts was conducted with a Hysitron-Bruker TI980 Nanoindenter. A conospherical tip, calibrated with a standard fused quartz, with a radius of 890 nm was used. For the nano-mechanical analysis of the suction-cast $Zr_{65}Cu_{25}Al_{10}$ bulk MG, the surface of a cross-sectional cut of a 2 mm diameter MG rod was prepared by a grind-and-polish treatment. This started with sandpaper of decreasing roughness, followed by diamond-based (3 μm and 1 μm) and 50 nm-SiO-particle suspensions, and was finished by rinsing with water. After these preparatory steps, the polished surface was characterized by nanoindentation mapping at several sites that are located within 0.3 mm from the rod's as-cast surface, which is roughly parallel to the y-direction of the maps. A Silicon ⟨100⟩ wafer, serving as a reference for the indenter's resolution limit under the given experimental conditions, is tested without further surface treatment.

A TEM lamella was lifted out using a dual-beam focused ion beam (Thermo Fisher Scientific Helios Nanolab 600i) instrument and mounted on a Cu grid. The lamella was thinned down at 30 kV accelerating voltage with a Ga ion beam using a current range from 2.5 to 0.8 nA. A final thinning at 5 kV and 43 pA, and cleaning at 2 kV and 16 pA were performed to remove surface damage from coarse milling steps at higher energy (30 kV). STEM imaging and EDS were carried out in a probe-aberration corrected Titan Themis 60–300 (Thermo Fisher Scientific) instrument at a beam semi-convergence angle of 17 mrad. A beam current of 70 pA was employed for imaging and 200 pA for STEM-EDS. The STEM-EDS spectrum images were acquired with four synchronized EDS detectors (ChemiSTEM). A pixel size of 2 nm and total acquisition time of 1.75-2 h were chosen to collect the drift corrected STEM-EDS data. The elemental maps were quantified with the Velox (Thermo Fisher Scientific) software using a standard-less Cliff-Lorimer quantification procedure.

3. Results

3.1. Nano-mechanical mapping of a Si reference

Prior to any examination of the Zr-based bulk MG, the instrument resolution of the nano-mechanical measurements in terms of the machine-intrinsic spread in the reduced indentation modulus, E, and the sample height, h, was determined on a Si-wafer. First, the topography was probed with the indenter tip at a contact force of 0.5 μN. Subsequently, the same area was characterized by elastic indents separated by 30 nm in both the vertical and horizontal direction. With a maximum load of 75 μN, this resulted in a contact radius of 53 nm at which E was determined.

Fig. 1 displays a probed area of 4 × 4 μm^2 on the Si-wafer. This area is directly comparable in size to the probed areas on the MGs we discuss later. Excess modulus values (E >200%) amounting to 1% of the indents were deemed erroneous and excluded from the analysis (white pixels in Fig. 1a). Since the topography scan is recorded with a higher data-point density, the number of pixels was reduced by averaging to the pixel density of the modulus map to facilitate a direct point-to-point comparison. The resulting variations in relative modulus and topography are quantified by fitting their histograms to a Gaussian exponential function (see Fig. 1c and d), yielding absolute values in standard deviation of 3.7% in modulus and 0.2 nm in height. These values reflect the resolution limit of the instrument under the specified experimental conditions. Fig. 1e depicts the normalized modulus as a function of normalized topography for the Si-wafer, where data sets have been normalized according to $X_N = (X - \min(X))/(\max(X) - \min(X))$. The cross-correlation is quantified by the squared residual, R^2, and the Pearson correlation coefficient, ρ, which is sensitive to linear correlations. The cross-correlation for the Si-reference has an insignificant R^2 of 0.03 and a ρ-value of -0.12, demonstrating the absence of any detectable linear correlation between topography and modulus.

3.2. Elastic microstructure of a Zr-based bulk MG

Following the determination of the system resolution, the Zr-based bulk MG was nano-mechanically mapped. A representative example of the resulting nano-mechanical response of the MG is shown in Fig. 2, where the connected indentation map consists of a total of 121 × 121 indents evenly spaced at 50 nm. Their maximum load was 75 μN, corresponding to a contact radius of 61 nm. In Fig. 2a the indentation modulus is plotted as a function of lateral position x and y. The distinct features in the map lead to a non-symmetric distribution ranging from −30% to +40% relative to the average indentation modulus (see Fig. 2c). The value for the standard deviation is of 13.2% in absolute percentage, more than a factor of three above the resolution limit of the instrument. The topography of the corresponding area was probed with the indenter tip at a contact force of 0.5 μN and is displayed in Fig. 2b. It exhibits a standard deviation of 3.8 nm, which is an order of magnitude larger than the system resolution.

The height data shows similar deviations from a normal distribution as the modulus data (Fig. 2d), but more importantly a comparison of the distinct local features in modulus and topography by visual analysis suggests a correlation. A plot of the normalized

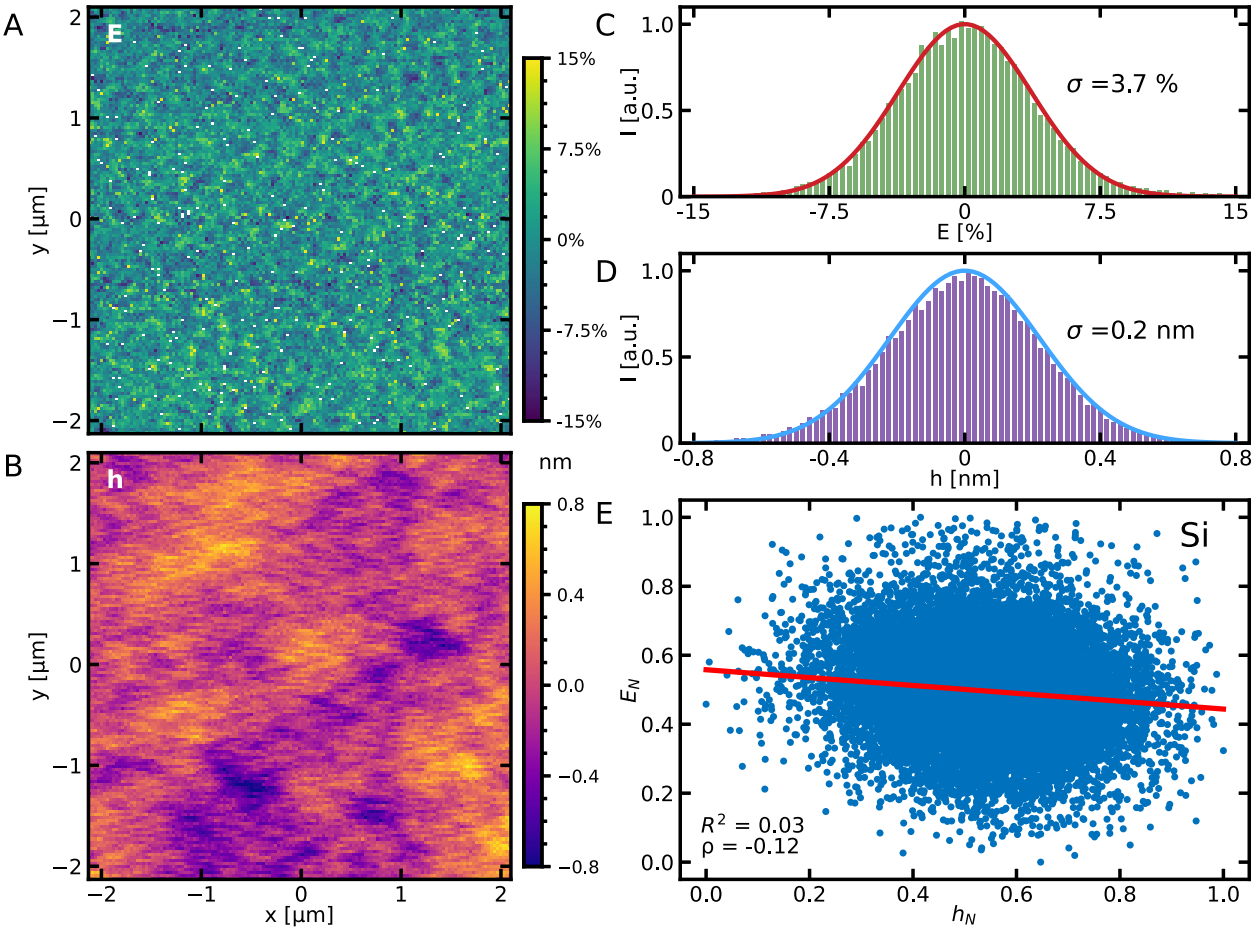

Fig. 1. Modulus (A) and topography (B) as functions of lateral position for a Si-wafer measured by nanoindentation, serving as a reference reflecting the instrument resolution. Panels (C) and (D) show the distributions of these mapped quantities together with the standard deviation σ. Panel (E) depicts the cross-correlation of modulus and topography for the Si-wafer. The linear correlation is quantified by the Pearson correlation coefficient ρ, and the squared residual R^2 of a linear fit to the data (red line). (For interpretation of the references to colour in this figure legend, the reader is referred to the web version of this article.)

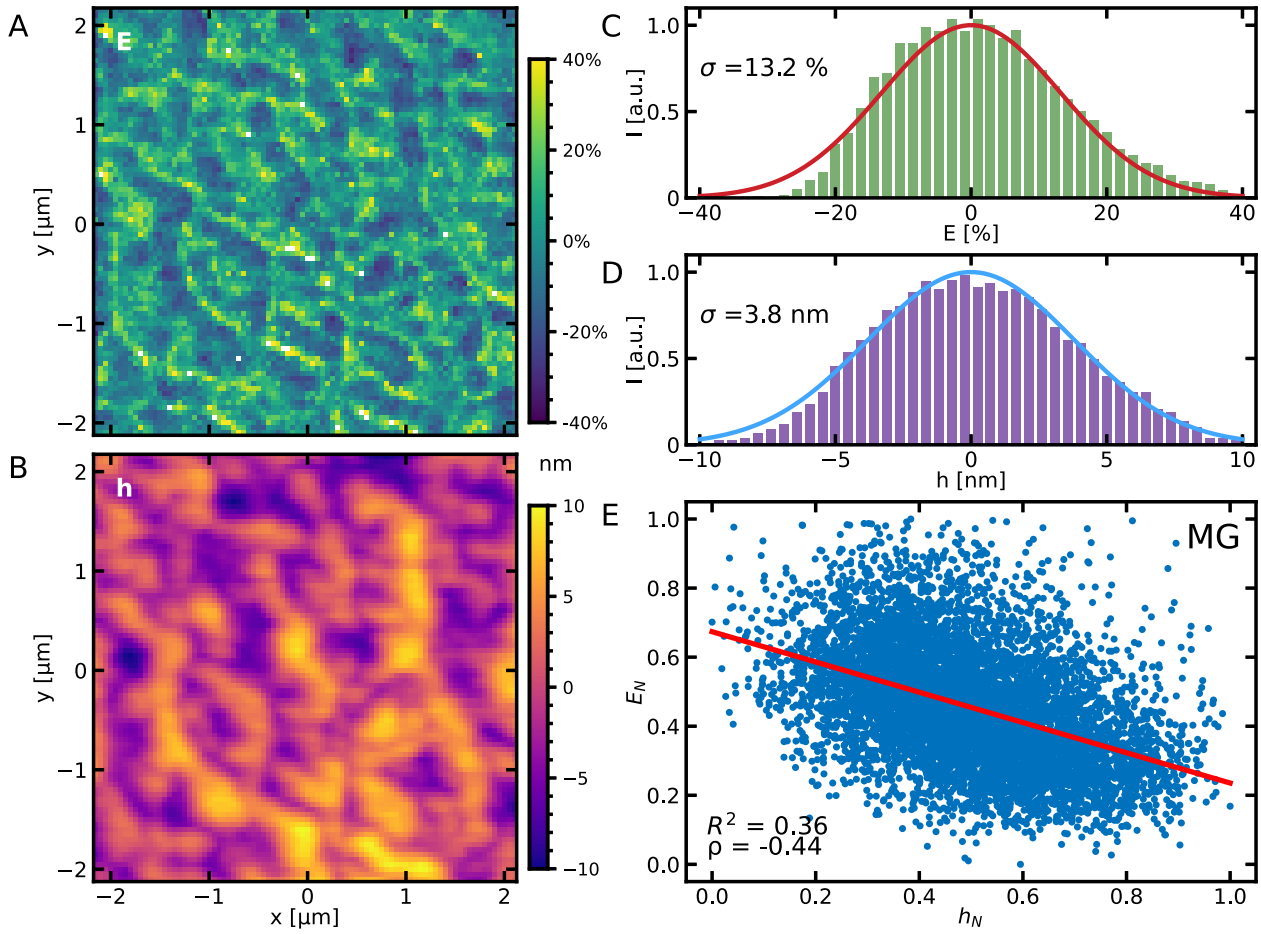

Fig. 2. Modulus (A) and topography (B) as functions of lateral position for a polished Zr-based bulk MG measured by nanoindentation. Panels (C) and (D) show the distributions of these mapped quantities together with the standard deviation σ. Panel (E) depicts the cross-correlation of modulus and topography for the Zr-based MG. The linear correlation is quantified by the Pearson correlation coefficient ρ, and the squared residual R^2 of a linear fit to the data (red line). (For interpretation of the references to colour in this figure legend, the reader is referred to the web version of this article.)

modulus as a function of normalized topography in Fig. 2e confirms this observation. The polished MG exhibits $R^2 = 0.36$ and $\rho = -0.44$, indeed indicating a (negative) linear correlation of the two quantities (Fig. 2e). We understand the negative trend to originate from the fact that elevated surface features yield an apparent elastically more compliant response. However, since the Young's modulus generally scales positively with the hardness [20], regions of lower modulus are expected to have a lower height value after the surface polishing procedure, not a higher value as seen here. The reason for the observed behavior is found in the local tip-sample interaction: Given the variation in local height by some nm, it is important to realize that the tip-sample interaction strongly differs from the idealized approach for modulus assessment, where a rigid sphere interacts with an infinitely flat surface. Instead, the influence of local curvature needs to be taken into account to yield representative modulus data [21].

Since the sample cannot be treated as an ideally flat plane but instead exhibits significant local topography variations, as a next step, we correct for this effect. Local gradients hardly affect the modulus assessment in our case [see supplementary information (SI)], while local curvature is observed to have a major impact. To this end, the curvature for two contacting bodies is taken into account by the equivalent radius, $R_{eq} = R_t(1 - 2R_tG + R_t^2K)^{-\frac{1}{2}}$, based on the tip's radius, R_t, and the surface's Gaussian and mean curvature, K and G [21,22] (see SI for details). By assuming Hertzian contact mechanics, a purely elastic response, and a local R_{eq} instead of a constant tip radius, the corrected modulus, E_c, can be deduced by $E_c = E\sqrt{\frac{R_t}{R_{eq}}}$. The effect of the curvature correction on the modulus data is shown in Fig. 3. Local features that visually resembled the topography are significantly reduced by the correction (see Fig. 3a). The resulting corrected modulus, ranging from −25% to +25% relative to the average, is described more accurately by a normal distribution function than the uncorrected data with a standard deviation of 10.3% (Fig. 3b) in absolute percentage. Plotting the normalized, curvature-corrected modulus as a function of normalized topography clearly demonstrates how the modulus data is corrected for the effect of topography (Fig. 3c). Both considered parameters, the Pearson coefficient and squared residuals, are effectively zero.

As a next step, we quantify the structural features observed in topography and corrected indentation modulus. This is achieved by analyzing the degree of autocorrelation and quantifying the characteristic length scale ξ with a radial autocorrelation function that reflects the correlation intensity as a function of radius, $\zeta(r)$. It measures the degree of correlation by the average difference for any pair of quantity X separated by distance r, where X is either modulus E or sample height h: $\zeta(r) = (X(r') - \bar{X}(r\prime + r))^2$. Thus, $\zeta(r)$ is small for distances r with strong average autocorrelation, while a large $\zeta(r)$ indicates dissimilarity of the quantity at distance r.

Fig. 4 summarizes the results for $\zeta(r)$ for both E_c and h, where $\zeta(r)$ increases with increasing radial distance, approaches a

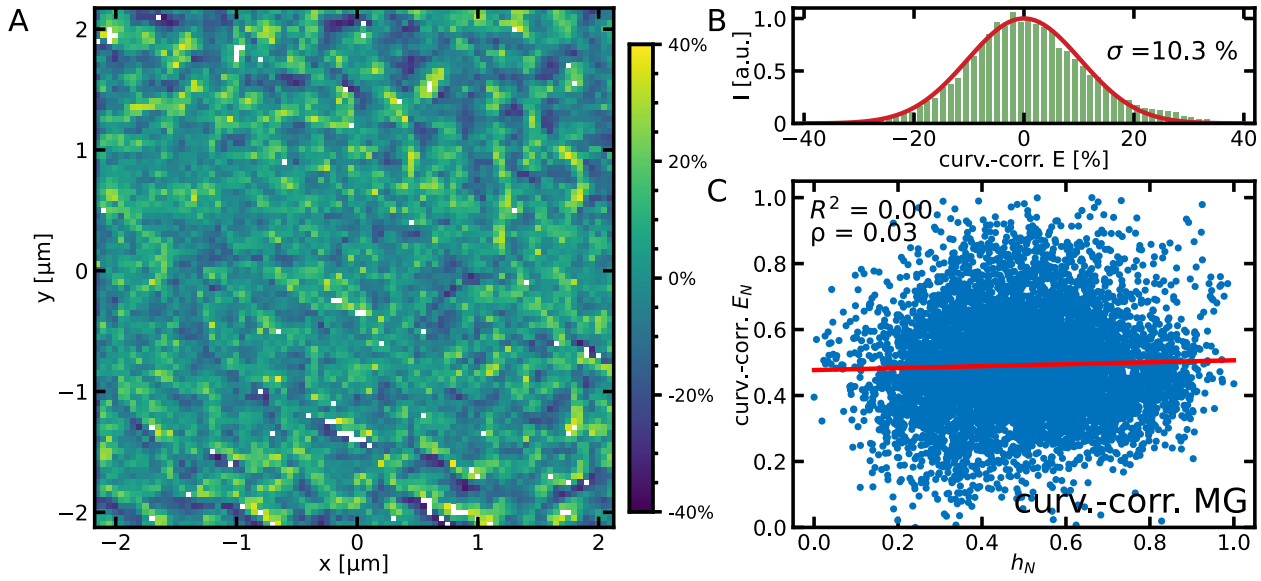

Fig. 3. Corrected modulus (A) as a function of lateral position for a polished Zr-based bulk MG measured by nanoindentation. Panel (B) shows the distribution of the corrected modulus together with the standard deviation σ. Panel (C) depicts the cross-correlation of corrected modulus and topography for the polished Zr-based MG. The linear correlation is quantified by the Pearson correlation coefficient ρ, and the squared residual R^2 of a linear fit to the data (red line). (For interpretation of the references to colour in this figure legend, the reader is referred to the web version of this article.)

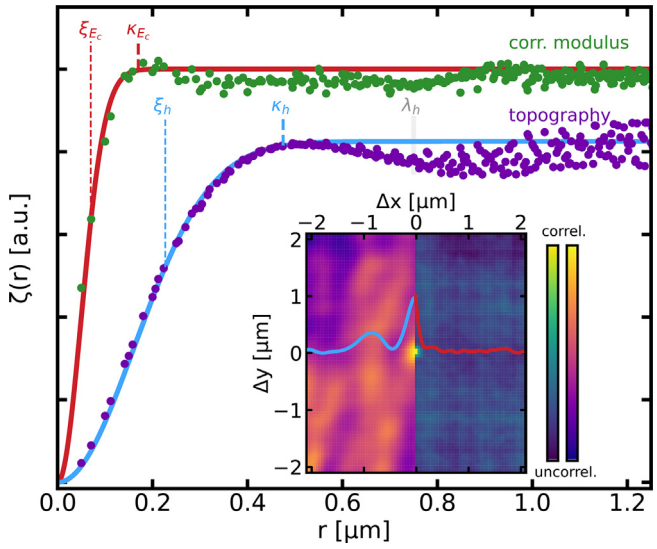

Fig. 4. Autocorrelation functions for corrected modulus as shown in Fig. 3 and topography as in Fig. 2 of the polished Zr-based bulk MG. Full lines correspond to fits of a stretched exponential function to the radial autocorrelation data. The inset shows the product autocorrelation of topography (left) and corrected modulus (right) with an overlay of the line profile along the x-direction at Δy = 0 as colored lines.

maximum value followed by shallow minima at intermediate distances, until levelling off at a final plateau value. While the shape of $\zeta(r)$ is qualitatively similar for both quantities, the positions of features differ for E_c and h and offer measures for their individual characteristic length scales. These can be deduced from the position of the first maximum, κ_X, indicating the smallest length scale at which the quantity shows average decorrelation, and the first minimum, λ_X, which indicates the periodicity of reoccurring features. For the topography, these values are identified as $\kappa_h \approx$ 475 nm and $\lambda_h \approx$ 750 nm. For the corrected modulus, the length scale of decorrelation amounts to κ_{E_c} = 170 nm (κ_E = 220 nm without correction), followed by minor correlation fluctuations in the radial range from 250 nm to 850 nm. It is consequently not possible to reliably quantify any λ_{E_c} with the present data.

To facilitate a comparison to length scales in the literature, we fit the initial evolution of the normalized radial autocorrelation function $\zeta(r)$ with a stretched exponential function, $f_\zeta(r) = 1 - e^{-\left(\frac{r}{\xi_X}\right)^\beta}$ with the characteristic length scale, ξ_X, and the shape parameter, β, as free fitting parameters. ξ_X reflects the distance over which the degree of correlation drops to $1/e$, resulting per definition in a shorter length scale than the maximum criterion and being therefore a different measure than κ_{E_c} derived from $\zeta(r)$. The fitted decorrelation length scales for E and h of the Zr-based MG amount to ξ_{E_c} = 70 nm (ξ_E = 97 nm without correction) and ξ_h = 227 nm, respectively.

As an alternative approach we test the mapped quantities by the product autocorrelation $P_X(\Delta x, \Delta y)$ for tendencies towards translational invariance. It is defined as the average of the product from a matrix multiplication of the mapped quantity, $X(x, y)$, with its shifted self, $X\prime(x + \Delta x, y + \Delta y)$. The result of the cross-correlation is shown in the inset of Fig. 4, where the purple-to-yellow and green-to-yellow data represent P_h and P_{E_c}, respectively. Additionally, the line profile of $P_X(\Delta x, \Delta y = 0)$ is plotted as lines normalized to values between 0 and 1. Generally, P_h shows a strong correlation approximately parallel to the y-axis of the maps, caused by the similarity of features along this dimension, while periodicity plays a major role along the orthogonal direction. The line profile (blue) plotted into the inset of Fig. 4 visualizes the initial decorrelation of the topographic structures over ca. 500 nm, followed by a range of strong correlation along the x-axis between 500 nm and 1000 nm. Its maximum coincides well with the radial correlation length scale λ_h. The product autocorrelation of the corrected modulus data, P_{E_c}, shows less features than the topography data. The initial decorrelation ranging over the first few pixels in the line profile (red), amounting to a decorrelation length scale in the range of 150 nm, is the strongest feature here, confirming the results from the radial autocorrelation: We do not observe a distinct periodicity for the corrected modulus, which underlines a successful decoupling of modulus and topography data by applying the topography-related correction.

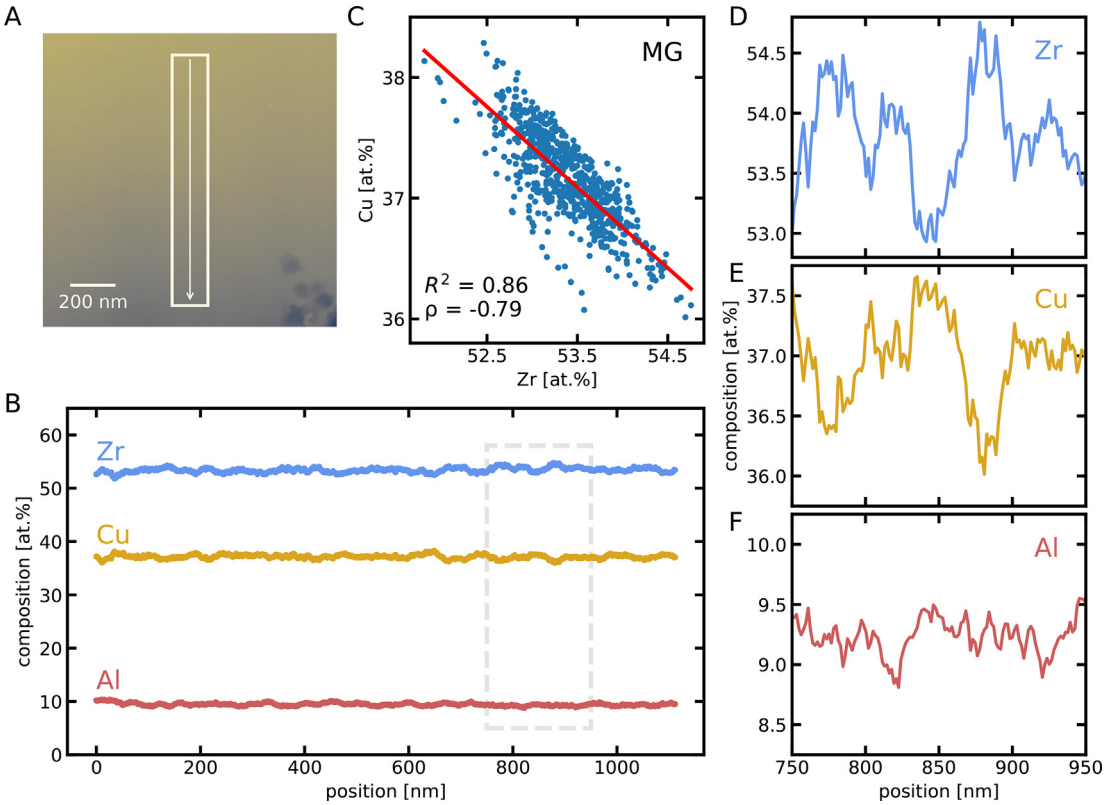

Fig. 5. Quantitative STEM-EDS-results for a Zr-based bulk MG with A) showing a LAADF-STEM image, where the box indicates the analysed region and the arrow the direction of the plotted data, which is shown as atomic percentage for the three elements Zr, Cu, and Al in B). Panel (C) depicts the cross-correlation of Zr- and Cu-EDS data from panel (B). The linear correlation is quantified by the Pearson correlation coefficient ρ, and the squared residual R^2 of a linear fit to the data (red line). Panel (D) to (F) depict details of the STEM-EDS line profiles of Zr, Cu, and Al for a randomly chosen region as marked by the dashed box in panel (B). (For interpretation of the references to colour in this figure legend, the reader is referred to the web version of this article.)

3.3. Quantitative transmission electron microscopy

As a next step, we test if a compositional modulation may be the origin of the observed elastic fluctuations. We pursued spatially resolved EDS elemental mapping in a STEM on a plane-view lamella (having the same out-of-plane axis as Fig. 2a or 3a) of the MG. Fig. 5a shows a low angle annular dark-field STEM (LAADF-STEM) image of the region where the STEM-EDS data were recorded. The rectangle in Fig. 5a and the arrow indicate the area and direction from which the integrated compositional line profiles shown in Fig. 5b were extracted. The LAADF-STEM image does not show any signs of contrast modulations on the length scale observed for the modulus fluctuations. The overall composition shown in Fig. 5b deviates from the nominal, which is due to an expected signal-contribution from the used TEM Cu-grid. A slight variation of composition can be seen in the line profiles for all elements. However, these modulations in chemical composition are only 1–3 atomic % (at.%), which is in the range of the resolution limit of STEM-EDS. Local variations in composition are subtle, but an indication for nm scale compositional variations is observed and most prominent in terms of an anti-correlation in the signals of Zr and Cu (Fig. 5c) as quantified by $R^2 = 0.86$ and $\rho = -0.8$. These are on a length scale of 30–50 nm by comparing the zoomed-in view of the profiles shown in Fig. 5d to 5f. Compositional modulations and an anti-correlation of elemental species at such scales have indeed been reported and are ascribed to miscibility gaps in the undercooled liquid [23]. However, the corresponding fluctuations emerge at a smaller length scale and are too weak in magnitude to account for the ±25% observed variation in mechanical modulus observed here.

4. Discussion

At this stage, we have demonstrated the existence of an intrinsic elastic decorrelation length in a Zr-based bulk MG by deconvoluting the nano-mechanical contact measurements from local curvature effects. The obtained decorrelation length is irrespective of the quantification method ($\xi_{E_c} = 70$ nm, $\kappa_{E_c} = 170$ nm) substantially above any structural length scale known for a monolithic MG. In direct contrast to the $Zr_{58.5}Cu_{15.6}Ni_{12.8}Al_{10.3}Nb_{2.8}$ investigated by Tsai et al. [13], κ_{E_c} is ∼ 10% larger (170 nm vs 150 nm), which is likely an underestimated difference because a topography-modulus deconvolution that would reduce the obtained value was not applied in Ref. [13]. In view of the strong evidence of elastic fluctuations at the several nm-scale revealed with AFM-methods we add here the second demonstration of an one-order-of-magnitude larger correlation length, underlining the existence of a hierarchical landscape of elastic heterogeneity for MGs.

What could the origin of this hierarchical elastic microstructure be? To address this question, we will consider the low and high length-scale extremes.

At the low nm-scale, AFM methods probe length scales based on local fluctuations in mechanical damping behavior that have been shown to decrease with the annealing state of the MG [8,9], similar to the case of ultrastable MGs [24]. At the same time, the temporal evolution of these length scales shows a temperature-dependence that yields activation energies reminiscent of the β-process [9]. This suggests that such length scales may be representative of the evolving heterogenous microstructure that is comprised of minimally frustrated structural motifs, such as (system spanning) icosahedral or Frank-Kaspar substructures, and a more frustrated

component, as seen in atomistic simulations of model binary glasses. It is within the latter frustrated regions that thermally-activated stress relaxation processes have been observed [25]. With time its evolution into well-relaxed structures must then underly the correlation lengths that reduce upon annealing. This picture is very compatible with numerous atomistic simulation studies that have quantified such a structural partitioning in model glass systems [26].

At the larger length scales of many tens of nm, the situation is less clear. In view of the complex multi-component chemistry of the alloys, liquid–liquid demixing is a potential reason for the observation of elastic property fluctuations. By diffusion-controlled decomposition during undercooling, phase separation such as spinodal decomposition is promoted, which can introduce significant compositional fluctuations of the solvent species with length scales of approx. 50–70 nm [19,23,27], a finding that is in general accordance with the Cahn-Hilliard theory [28]. We test this scenario by spatially mapped STEM-EDS and observe compositional fluctuations on a decorrelation length scale of about 50 nm, matching these previous findings in the literature. This proves, however, that a compositional length scale similar to that of the elastic fluctuations does not exist in the MG. The connected compositional variations remain close to the resolution limit of the technique at 1-3 at.%. While properties such as plasticity and glass-forming ability are highly sensitive to compositional variations even below the resolution limit [29,30], elasticity is not a quantity known to be strongly affected [31]. Further, the observed extremes in modulus of ±25% would rather correspond to moduli of elemental Cu or Al, connected to compositional changes that would be well detectable by STEM-EDS. We thus exclude modulations in composition as well as nano-crystallites as the source for the observed modulus fluctuations.

Consequently, the elastic fluctuations must arise from structural variations that we primarily regard as density fluctuations. At this stage, we propose that these density fluctuations emerge during the solidification process in connection to the directional and constrained cooling. For a cylindrical rod, the outermost shell of the material solidifies first, resulting in a radial-symmetric and non-monotonic stress field that arises due to the temperature-dependent elastic properties of the material [32]. Indeed, the existence of residual tensile and compressive stresses was demonstrated experimentally for a Zr-based MG rod of ca. 7 mm diameter and these amount to 100–300 MPa based on residual strains of up to 0.3% [33]. We propose that our nanoscopic observations are a local manifestation of the cooling-induced macroscopic stress field.

Interestingly, quite different mechanisms can be at the origin of the locally resolved phenomenon, including stress-induced local rejuvenation or a volume-frustration of structural motifs. In a scenario of local rejuvenation, we consider solidification-induced stresses that can yield strain in the low-percentage range along the radial direction due to the specific volume mismatche between the liquid and glass [34]. To release strain energy, and in accordance with the fluctuation–dissipation-theorem, plastic processes create less relaxed environments, and thus locally rejuvenated regions in the wake of the progressing solidification front. The length scale of such alternating stress relaxation is governed by the solidification-induced stress field and the cooling rate. The second scenario connects to the intrinsic volume frustration existing in the well-relaxed network of structural motifs and is therefore intimately linked to the discussed microscopic length scale at the nanometer range: To allow for the formation of these more relaxed regions, the surrounding material must compensate and arrange in structures that are more frustrated, just as the case for clusters formed on the nm scale and observed by AFM techniques [7–12,14,15].

Even though it remains unclear if locally rejuvenated regions due to stress-induced plastic relaxation or an extended range of a minimally frustrated network underlies the structural fluctuations, we concur that both can result in distinct differences in the local density of the MG. Since density holds a reasonably strong influence over the elastic properties of an MG, even subtle changes in density have a major impact on the modulus. This becomes obvious when considering that the density of an MG decreases by only 5% when heating through the glass transition [34], while the modulus decreases by orders of magnitude. Thus, density is a property that can, even by comparably small variation, amount for the observed changes in elastic modulus of up to ±25%. Another important argument for the proposed solidification-induced structural variations is given by the directionality of the modulus variations (Fig. 2a and Fig. 4, and in Ref. [13]) that suggest a connection to the concentrically progressing cooling front during the suction casting process.

A final question is, why existing literature, apart from the work on a bulk MG [13], has not given any evidence for this $\sim$ 100 nm range length scale in addition to the microscopic length scale of a few nm. Central to this is that AFM-based studies do not probe surfaces that are influenced by a solidification front. Instead, studied surfaces originate from sputter deposition [7–9,15], as-cast surfaces that were perpendicular to the solidification direction [12], and ribbons where no geometric volume confinement exists [10,11,14]. A length scale that is strongly affected by cooling constraints due to the casting process can thus not emerge in these cases. To strengthen our argument that length scales of the order of 100 nm are not observed under unconstrained cooling conditions, we also conducted spatially resolved modulus mapping by nanoindentation on the freely cooled surface of an as-cast Pd-based ribbon over an area of 4×4 μm^2. This surface does not indicate the existence of modulus fluctuations as observed for the bulk MG reported here. Instead, the probed area is similarly smooth as the Si-wafer with a standard deviation of 0.2 nm reflecting the resolution limit, and the modulus shows a narrower distribution than the bulk MG with a standard deviation of 5.9% without any indications for a decorrelation length scale. Whilst this supports our reasoning, further characterization in connection to cooling rate, geometrical constraints, as well as major alloy components, as for example by studying Pd- or La-based MGs, are needed to better quantify the origin of the observed elastic microstructure. These necessary steps promise significant strides towards elastic length-scale design that may constitute a novel way of property control of MGs.

5. Summary

In summary, we pursued high-throughput spatially resolved modulus mapping on a monolithic Zr-based bulk MG combined with analytical STEM. The nano-mechanical data reveals a curvature-corrected intrinsic modulus fluctuation of ±25% with a characteristic length scale of ca. 170 nm. Spatially resolved STEM-EDS elemental mapping does not reveal any compositional signatures at the modulus correlation length. We can therefore exclude chemical phase separation, such as spinodal decomposition, as an origin of the elastic microstructure and argue that the correlation length originates from density fluctuations that emerge during the solidification process. These findings strengthen the view of a hierarchy of elastic length scales in MGs that entail an unexplored opportunity of targeted microstructural tuning at different scales.

6. Author statement

R.M. designed the study. B.R. and C.O. contributed to the nano-mechanical measurements. B.R. developed and conducted the nano-mechanical analysis. S.M.D. prepared the TEM lamella and S.M.D. and C.H.L. conducted the STEM-EDSM measurements and analysis. B.R. and R.M. wrote the manuscript. All authors contributed to the interpretation and presentation of the results.

Data availability

Data is available at 10.5281/zenodo.7818225.

Declaration of Competing Interest

The authors declare that they have no known competing financial interests or personal relationships that could have appeared to influence the work reported in this paper.

Acknowledgements

The authors gratefully acknowledge financial support by the German Aerospace Center (Grant No. 50WM2158), the European Union's Horizon Europe Framework Programme (HORIZON) under the Marie Skłodowska Curie grant agreement (No. 101063523), and BAM's Adolf Martens Postdoctoral Fellowship.

Appendix A. Supplementary material

Supplementary data to this article can be found online at https://doi.org/10.1016/j.matdes.2023.111929.

References

[1] H. Sheng, W. Luo, F. Alamgir, J. Bai, E. Ma, Atomic packing and short-to-medium-range order in metallic glasses, Nature 439 (7075) (2006) 419–425.
[2] U.R. Pedersen, T.B. Schrøder, J.C. Dyre, P. Harrowell, Geometry of slow structural fluctuations in a supercooled binary alloy, Phys. Rev. Lett. 104 (10) (2010) 105701.
[3] P.M. Derlet, Correlated disorder in a model binary glass through a local SU(2) bonding topology, Phys. Rev. Mater. 4 (12) (2020) 125601.
[4] P.M. Derlet, R. Maass, Emergent structural length scales in a model binary glass - the micro-second molecular dynamics time-scale regime, J. Alloy Compd. 821 (2020) 153209.
[5] P.M. Derlet, R. Maass, Thermal processing and enthalpy storage of a binary amorphous solid: a molecular dynamics study, J. Mater. Res. 32 (14) (2017) 2668–2679.
[6] C.Y. Liu, R. Maass, Elastic fluctuations and structural heterogeneities in metallic glasses, Adv. Funct. Mater. 28 (30) (2018) 1800388.
[7] Y.H. Liu, D. Wang, K. Nakajima, W. Zhang, A. Hirata, T. Nishi, A. Inoue, M.W. Chen, Characterization of nanoscale mechanical heterogeneity in a metallic glass by dynamic force microscopy, Phys. Rev. Lett. 106 (12) (2011).
[8] Y. Yang, J.F. Zeng, A. Volland, J.J. Blandin, S. Gravier, C.T. Liu, Fractal growth of the dense-packing phase in annealed metallic glass imaged by high-resolution atomic force microscopy, Acta Mater. 60 (13–14) (2012) 5260–5272.
[9] F. Zhu, H.K. Nguyen, S.X. Song, D.P.B. Aji, A. Hirata, H. Wang, K. Nakajima, M.W. Chen, Intrinsic correlation between beta-relaxation and spatial heterogeneity in a metallic glass, Nat. Commun. 7 (2016) 11516.
[10] D.P. Wang, J.C. Qiao, C.T. Liu, Relating structural heterogeneity to beta relaxation processes in metallic glasses, Mater. Res. Lett. 7 (8) (2019) 305–311.
[11] M. Gao, J.H. Perepezko, Mapping the viscoelastic heterogeneity at the nanoscale in metallic glasses by static force spectroscopy, Nano Lett. 20 (10) (2020) 7558–7565.
[12] P. Ross, S. Kuchemann, P.M. Derlet, H.B. Yu, W. Arnold, P. Liaw, K. Samwer, R. Maass, Linking macroscopic rejuvenation to nano-elastic fluctuations in a metallic glass, Acta Mater. 138 (2017) 111–118.
[13] P. Tsai, K. Kranjc, K.M. Flores, Hierarchical heterogeneity and an elastic microstructure observed in a metallic glass alloy, Acta Mater. 139 (2017) 11–20.
[14] H. Wagner, D. Bedorf, S. Kuchemann, M. Schwabe, B. Zhang, W. Arnold, K. Samwer, Local elastic properties of a metallic glass, Nat. Mater. 10 (6) (2011) 439–442.
[15] N. Wang, J. Ding, P. Luo, Y.H. Liu, L. Li, F. Yan, Chemical variation induced nanoscale spatial heterogeneity in metallic glasses, Mater. Res. Lett. 6 (12) (2018) 655–661.
[16] D. Tonnies, K. Samwer, P.M. Derlet, C.A. Volkert, R. Maass, Rate-dependent shear-band initiation in a metallic glass, Appl. Phys. Lett. 106 (17) (2015) 171907.
[17] A.S. Argon, Physics of strength and plasticity, M.I.T. Press, Cambridge, MA, 1969.
[18] E. Arzt, Size effects in materials due to microstructural and dimensional constraints: a comparative review, Acta Mater. 46 (16) (1998) 5611–5626.
[19] R. Busch, S. Schneider, A. Peker, W.L. Johnson, Decomposition and primary crystallization in undercooled Zr41.2Ti13.8Cu12.5Ni10.0Be22.5 melts, Appl. Phys. Lett. 67 (11) (1995) 1544–1546.
[20] F. Zhu, S.X. Song, K.M. Reddy, A. Hirata, M.W. Chen, Spatial heterogeneity as the structure feature for structure-property relationship of metallic glasses, Nat. Commun. 9 (2018) 3965.
[21] A.C. Campbell, V. Buršíková, J. Martinek, P. Klapetek, Modeling the influence of roughness on nanoindentation data using finite element analysis, Int. J. Mech. Sci. 161 (2019) 105015.
[22] A.C. Fischer-Cripps, Nanoindentation, 3rd ed.2011.
[23] S. Schneider, P. Thiyagarajan, W.L. Johnson, Formation of nanocrystals based on decomposition in the amorphous Zr41.2Ti13.8Cu12.5Ni10Be22.5 alloy, Appl. Phys. Lett. 68 (4) (1996) 493–495.
[24] T. Dziuba, Y.S. Luo, K. Samwer, Local mechanical properties of an ultrastable metallic glass, J. Phys.-Condens. Mat. 32 (34) (2020) 345101.
[25] P.M. Derlet, R. Maass, Micro-plasticity in a fragile model binary glass, Acta Mater. 209 (2021) 116771.
[26] Y.Q. Cheng, E. Ma, Atomic-level structure and structure–property relationship in metallic glasses, Prog. Mater. Sci. 56 (4) (2011) 379–473.
[27] B.J. Park, H.J. Chang, D.H. Kim, W.T. Kim, K. Chattopadhyay, T.A. Abinandanan, S. Bhattacharyya, Phase separating bulk metallic glass: a hierarchical composite, Phys. Rev. Lett. 96 (24) (2006) 245503.
[28] C. Borchers, J. Schroers, R. Busch, Prediction of spinodal wavelength in continuously cooled metallic liquid, Ann. Phys. 18 (1) (2009) 4–12.
[29] Y.H. Liu, G. Wang, R.J. Wang, D.Q. Zhao, M.X. Pan, W.H. Wang, Super plastic bulk metallic glasses at room temperature, Science 315 (5817) (2007) 1385–1388.
[30] D. Wang, H. Tan, Y. Li, Multiple maxima of GFA in three adjacent eutectics in Zr–Cu–Al alloy system–a metallographic way to pinpoint the best glass forming alloys, Acta Mater. 53 (10) (2005) 2969–2979.
[31] W.H. Wang, The elastic properties, elastic models and elastic perspectives of metallic glasses, Prog. Mater. Sci. 57 (3) (2012) 487–656.
[32] L.C.E. Struik, Orientation effects and cooling stresses in amorphous polymers, Polym. Eng. Sci. 18 (10) (1978) 799–811.
[33] A.M. Korsunsky, T. Sui, E. Salvati, E.P. George, M. Sebastiani, Experimental and modelling characterisation of residual stresses in cylindrical samples of rapidly cooled bulk metallic glass, Mater. Des. 104 (2016) 235–241.
[34] K.C. Chow, S. Wong, H.W. Kui, The specific volumes of Pd40Ni40P20 in the liquid, glass, and crystallized states, J. Appl. Phys. 74 (9) (1993) 5410–5414.